



Multiphasic size-dependent growth dynamics of nanoparticle ensembles

Ji-Hyun Kim^{a,b,c,1}, Joodeok Kim^{d,e,1}, Byung Hyo Kim^{d,e,f,1}, Sanggeun Song^{g,h,1}, Jinyu Kang^{a,b,c,i} , Jinho Rhee^{d,e} , Donghee Kim^{a,b,c,i}, Hoje Chun^j, Hyesung Choi^{d,e}, Hyungjin Cho^f, Yongjoon Kim^f, Jae Won Jung^f, Youngju Son^{d,e}, Junhyeok Jung^{d,e}, Kunwoo Park^{d,e}, Sungho Jeon^k, Minhoo Lee^{a,b,c,i} , Byungchan Han^l , Won Chul Lee^k, Dongjun Kim^{d,e} , Taeghwan Hyeon^{d,e,2}, Jaeyoung Sung^{a,b,c,i,2} , and Jungwon Park^{d,e,l,m,2}

Affiliations are included on p. 10.

Edited by Qian Chen, University of Illinois at Urbana Champaign, Urbana, IL; received December 3, 2024; accepted April 22, 2025 by Editorial Board Member Peter J. Rossky

Colloidal nanoparticles are of great interest in modern science and industry. However, the thermodynamic mechanism and dynamics of nanoparticle growth have yet to be understood. Addressing these issues, we tracked hundreds of in-situ growth trajectories of a nanoparticle ensemble using liquid-phase TEM and found that the nanoparticle growth, including coalescence, exhibits nanoparticle size-dependent multiphasic dynamics, unexplainable by current theories. Motivated by this finding, we developed a model and theory for an ensemble of growing nanoparticles, providing a unified, quantitative understanding of the time-dependent mean and fluctuation of nanoparticle size and size-dependent growth rate profiles across various nanoparticle systems and experimental conditions. Our work reveals that the chemical potential in a small nanoparticle strongly deviates from the Gibbs–Thomson equation, shedding light on how it governs the size-dependent growth dynamics of nanoparticles.

in-situ liquid-phase TEM | nanoparticle growth trajectories | monomer chemical potential | size-dependent growth rate | nanoparticle coalescence

Nanoparticle properties can be tuned by their size and shape, which makes them highly attractive materials in both science and industry (1–3). For the last three decades, tremendous effort has been devoted to synthesizing monodisperse nanoparticles of controlled sizes, shapes, and compositions (4–6), not only for investigating their unique physico-chemical properties but also for various applications such as quantum-dot-enhanced display (7) and nanocatalyst (8). Despite extensive research, the thermodynamic mechanism of monodisperse nanoparticle formation has not been clearly understood, and quantitative understanding of nanoparticle growth dynamics has not been achieved (9–11).

The classical nucleation theory (CNT) based on the Gibbs–Thomson equation has provided a central basis for understanding crystallization dynamics for more than a century (12–15). However, the CNT has a limitation in that it cannot explain the formation of monodisperse nanoparticles (16, 17). Early work by Frenkel (18) showed that the monodispersity of colloidal particles at a stationary state under supersaturation is not consistent with the equilibrium size distribution predicted by the CNT. Recently, a nonequilibrium nanoparticle growth process was recorded in real time by liquid-phase transmission electron microscopy (TEM) (19–23). Liquid-phase TEM of individual nanoparticles revealed that the nanoparticle growth pathway is far more complex than assumed in the classical crystallization model (24–28). For example, TEM studies presented direct evidence of nanoparticle coalescence and its contribution to the nanoparticle size distribution (29). They also revealed that a specific surface selectively develops, while growth of other surfaces is suppressed, to form faceted nanoparticles, in metal nanoparticles (30, 31). Several kinetic models have been proposed to explain the growth dynamics of nanoparticles (9, 16, 17, 32–35). Talapin et al. (32) and separately Rempel et al. (35) investigated dynamics of nanoparticle size focusing, using diffusion-limited and reaction-limited growth models. Each of these approaches provided a new qualitative picture of nanoparticle size-focusing dynamics. However, a unified, quantitative understanding of the nanoparticle growth dynamics has yet to be achieved. This is primarily due to lacking a realistic model of a nanoparticle and a rigorous theory describing nanoparticle growth dynamics, in addition to the lack of large sets of experimental data showing the detailed features of individual growth trajectories of nanoparticle ensembles (19–21).

Here, we developed an advanced in-situ liquid-phase TEM and monitored an ensemble of platinum nanoparticle growth trajectories. This direct observation reveals that nanoparticles with radii of a few nanometers exhibit size-dependent growth dynamics with multiple

Significance

We first observe in-situ, real-time growth trajectories of hundreds of colloidal nanoparticles with radii of a few nanometers and find anomalous size-dependent growth dynamics that cannot be explained by the classical nucleation theory or other currently available theories. We present a nanoparticle model and statistical mechanical theory that provide a unified, quantitative explanation of both the mean and variance of the sizes of growing nanoparticles and their size-dependent growth rate profiles at various times across diverse systems and experimental conditions. This work reveals that the chemical potential in a nanoparticle exhibits nonmonotonic size dependence, deviating strongly from the Gibbs–Thomson equation for small nanoparticles. It also uncovers how this leads to anti-Ostwald-ripening growth dynamics, observed across various small nanoparticle systems.

The authors declare no competing interest.

This article is a PNAS Direct Submission. Q.C. is a guest editor invited by the Editorial Board.

Copyright © 2025 the Author(s). Published by PNAS. This open access article is distributed under [Creative Commons Attribution-NonCommercial-NoDerivatives License 4.0 \(CC BY-NC-ND\)](https://creativecommons.org/licenses/by-nc-nd/4.0/).

¹J.-H.K., J.K., B.H.K., and S.S. contributed equally to this work.

²To whom correspondence may be addressed. Email: thyeon@snu.ac.kr, jaeyoung@cau.ac.kr, or jungwonpark@snu.ac.kr.

This article contains supporting information online at <https://www.pnas.org/lookup/suppl/doi:10.1073/pnas.2424950122/-/DCSupplemental>.

Published June 4, 2025.

kinetic phases, markedly different from Ostwald ripening. In each of the phases, the mean and variance of nanoparticle size and the size dependence of nanoparticle growth rate exhibit their own distinct dynamics, and all these features are sensitive to chemical identities of nanoparticles and precursors of monomers. In addition, nanoparticles undergo coalescence with a strongly time-dependent rate that transiently surges and then vanishes. We found these experimental results unexplainable by current theories. Motivated by these findings, we developed a novel model of nanoparticles and a statistical mechanical, kinetic theory for an ensemble of growing nanoparticles. Our theory provides not only new physical insights into nanoparticle nucleation and growth dynamics but also a simultaneous, quantitative explanation of diverse experimental data, including time-dependent profiles of the mean, variance, and higher-order moments, from the 3rd to the 10th of nanoparticle size distribution as well as the size-dependent profiles of the nanoparticle growth rate, which shows a wild shape variation over time, for various nanoparticle systems under different experimental conditions. In doing so, we demonstrated that the time evolution of our new experimental observable, the nanoparticle size-dependent growth rate profile, provides direct information about the size dependence of the chemical potential in a nanoparticle and the time evolution of the monomer concentration.

Our work reveals the chemical potential of a monomer in a nanoparticle has a nonmonotonic size dependence with its maximum value at a critical nanoparticle size, differing from the Gibbs–Thomson equation underlying the CNT, according to which the monomer chemical potential monotonically decreases with the nanoparticle size. This discrepancy from the Gibbs–Thomson equation is caused by the strongly nonextensive free energy, originating from nanoparticle’s translational and rotational motion, configurational degeneracy, and edge interaction with the surrounding environment, neglected in the CNT. This nonclassical size dependency of the chemical potential causes a significant deviation of the nanoparticle growth dynamics from Ostwald ripening, which we found common across various small nanoparticle systems we investigated.

Results

In-Situ Nanoparticle Growth and Classification of Growth Trajectories. We observed an ensemble of growing metal nanoparticles in real time using liquid-phase TEM (Fig. 1A and Movies S1–S4). Multiple in-situ liquid-phase TEM movies were recorded, which show growth processes of individual Pt and Au nanoparticles, under different reaction conditions (*Materials and Methods*, Movies S1 and S2 for Pt nanoparticles from precursor Pt(acac)₂, Movie S3 for Pt nanoparticles from precursor Pt(COD)Cl₂, where Pt(acac)₂ has a platinum supplying rate higher than Pt(COD)Cl₂ (*SI Appendix*, Fig. S1 and Text S1), and Movie S4 for gold nanoparticles from precursor HAuCl₄). From these movies, we tracked growth trajectories of several hundred individual nanoparticles. To accurately track the size changes of hundreds of individual nanoparticles in the field of view of the in-situ TEM movies, we developed an integrated image processing method, which includes noise removal, edge-contrast optimization, and inconspicuous pixel removal to enhance edge contrast while efficiently reducing noise from instruments and solvent background (*Materials and Methods*, Fig. 1B and *SI Appendix*, Fig. S2) (36). The resulting binarized image series preserves the sizes and positions in the original liquid-phase TEM images and enables unbiased, high-throughput measurements of the size and shape of all tracked nanoparticles (Movies S1–S4 and *SI Appendix*, Figs. S3–S9). All growth trajectories that remained in our field

of view for 180 s in Movie S1, 84 s in Movie S3, and 193.5 s in Movie S4 are collectively presented in Fig. 1C.

We classified the growth trajectories of nanoparticles into two groups: one showing only monomeric growth (Group-A) and the other exhibiting both monomeric growth and coalescence growth (Group-B) (Fig. 1A and *SI Appendix*, Text S2). As these two groups exhibit qualitatively different growth dynamics, we analyzed them separately (34). Group-A, which undergoes monomeric growth, makes the dominant contribution to the size distribution; its size distribution is similar to the distribution of all nanoparticles, including Group-A and Group-B (*SI Appendix*, Fig. S10). For gold nanoparticles, we found that Group-B is strongly suppressed and only Group-A is observed in our experiment (*SI Appendix*, Text S3 and Movie S4).

Monomeric Growth Dynamics. Monomeric growth dynamics of nanoparticles is decomposable into multiple kinetic phases, which are distinct for each precursor as shown in Fig. 1E (Phase-I–V for platinum nanoparticles generated from precursor Pt(acac)₂, Phase-A–C for platinum nanoparticles from Pt(COD)Cl₂, with a slower monomer supply rate than Pt(acac)₂, and Phase-1–2 for gold nanoparticles generated from HAuCl₄). For platinum nanoparticle systems, the mean and variance of the nanoparticle size exhibit rapid growth in the initial phase, but slower growth in the next phase, and then rapid growth again in the subsequent phases. In comparison, the phase-to-phase variation in growth dynamics is less significant for the gold nanoparticle system (*SI Appendix*, Text S4 for the details of the phase-dependent mean and variance in each nanoparticle system). We also measured the size-dependent profile of nanoparticle growth rate and found that the size dependency of the growth rate shows highly dynamic phase-dependent behavior, which cannot be explained by Ostwald ripening or currently available theories (Fig. 2).

To explain these experimental results, we introduced a novel model of nanoparticle and developed a statistical mechanical, kinetic theory for a system of nanoparticles growing through diffusion-influenced reversible association with monomers in solution (*Materials and Methods*). This theory enables us to provide a simultaneous, quantitative explanation of all experimental results mentioned above (Figs. 1E and 2 C–E). Our nanoparticle model accounts for six essential characteristics of a nanoparticle. Four of these characterize physical properties such as monomer energy in the face and on the edge of the nanoparticle, relative to the monomer energy in the core, the shape and configurational degeneracy of the nanoparticle. The remaining two characterize the chemical properties, such as the monomer diffusion constant and the monomer association rate per nanoparticle surface area. We found the value of the shape parameter, which characterizes the geometry of a nanoparticle, little changes over time without showing a noticeable trend (*SI Appendix*, Figs. S11 and S12). Therefore, our analysis essentially involves only one time-dependent adjustable parameter, the monomer concentration in solution (*SI Appendix*, Fig. S13).

We note here that our model is a minimalistic representation of nonspherical nanoparticles with defects, growing through diffusion-influenced reversible association with monomers. Simplifying our model makes it impossible to achieve the quantitative explanation of our diverse experimental results. This indicates that the four physical and two chemical properties considered in our nanoparticle model are essential characteristics that determine the size distribution and growth dynamics of nanoparticles.

Remarkably, our theory can also make a prediction about the time profiles of the higher-order moments of the nanoparticle size distribution. With the optimized parameter values in Table 1, the theoretical predictions show excellent agreement with experimental

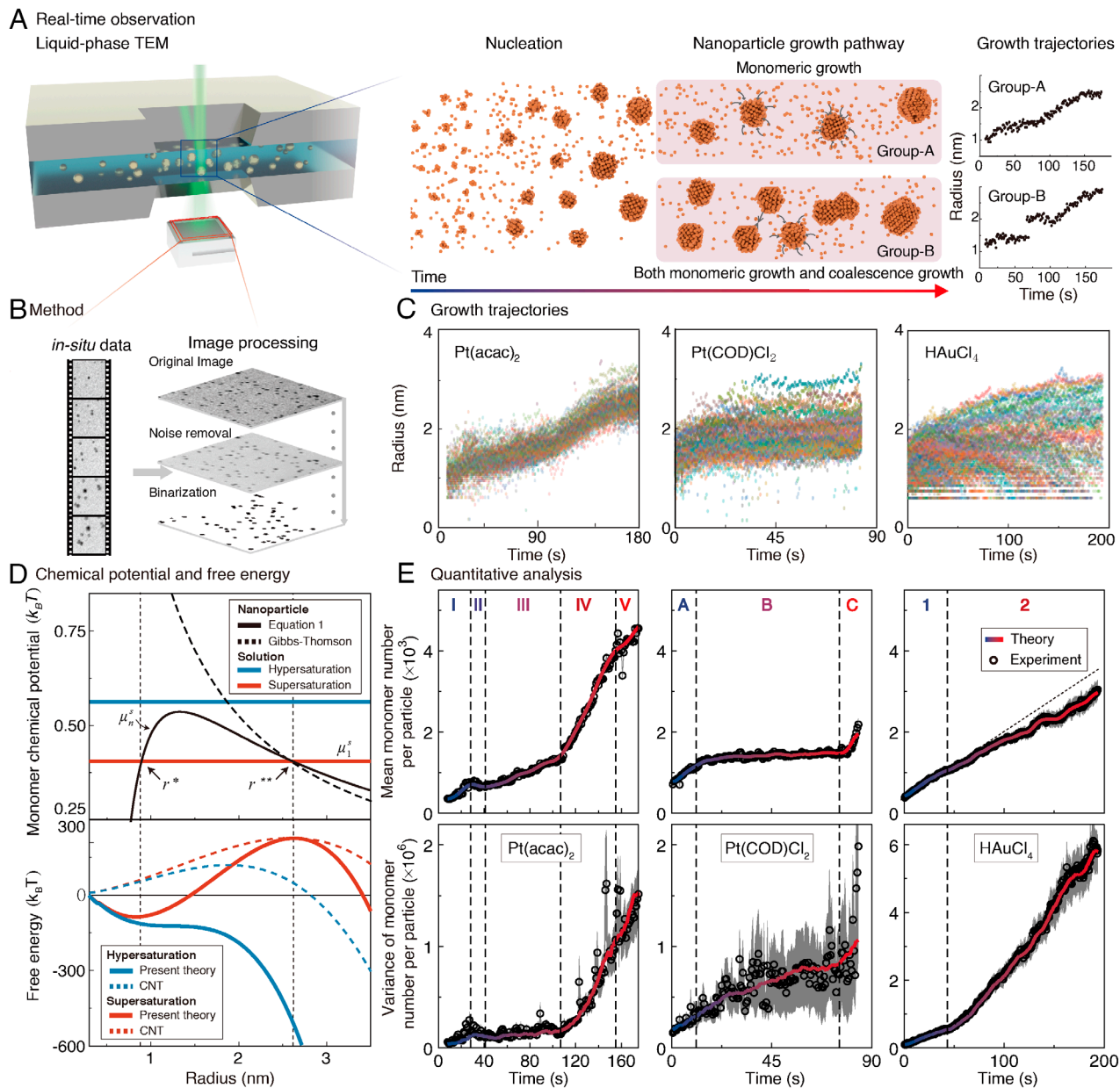


Fig. 1. Multiphasic growth dynamics of nanoparticle ensembles observed by liquid-phase TEM. (A) Schematic of our experimental measurement of individual growth trajectories of metal nanoparticle ensemble. (Left) real-time in-situ observation of nanoparticle growth using a liquid-phase TEM. (Center) Group-A showing only monomeric growth and Group-B exhibiting both monomeric growth and coalescence growth. (Right) the pathway-dependent growth trajectories for platinum nanoparticles. (B) Schematic of TEM image processing including noise removal, edge-contrast optimization, adaptive binarization, and inconspicuous pixel removal to convert in-situ TEM images into binarized images. (C) Individual growth trajectories of hundreds of metal nanoparticles obtained using different precursors. (Left) Pt(acac)₂. (Center) Pt(COD)Cl₂. (Right) HAuCl₄. (D, Top) Chemical potential, μ_n^s , of monomers in a nanoparticle, Eq. 1 (black solid line), the Gibbs-Thomson equation, SI Appendix, Eq. S10-10 (black dashed line), and chemical potential, μ_1 , of monomers in supersaturated solution (red line) and in hypersaturated solution (blue line). For the hypersaturated solution, μ_1 is larger than the maximum of μ_n^s . Absolute size focusing (anti-Ostwald ripening) occurs for nanoparticles with sizes close to r^* , while nanoparticles with size close to r^{**} undergo Ostwald ripening (SI Appendix, Text S5). (Bottom) The corresponding Gibbs free energy change associated with the formation of a nanoparticle from monomers, the present theory (solid line) and the CNT (dashed line): supersaturated solution (red) and hypersaturated solution (blue). (E) Comparison between theory and experiment for the mean and variance of the monomer number per particle: experimental results (circles) and theoretical results (lines). The gray-shaded area represents the SD at each time frame, estimated from one thousand bootstrap-sampled sets.

results for the time profiles of higher-order moments, from the 3rd to the 10th, at all times investigated (Fig. 3). This quantitative agreement further supports the validity of our model and theory.

The success of our model stems from its ability to capture all the essential microscopic degrees of freedom of nanoparticles and accurately assess their effects on the nanoparticle's free energy and chemical potential. In our nanoparticle model, we took into account the translation, rotation, and vibration motion of a nanoparticle, overlooked in the CNT, as well as its shape-dependent

electronic interactions with the surrounding environment through its faces and edges. In addition, we consider configurational degeneracy of a nanoparticle.

Starting from this model, we derive an accurate expression for the size-dependent chemical potential, μ_n^s , of monomers in a nanoparticle, which is given by

$$\beta(\mu_n^s - \mu_\infty^s) = \frac{c_1(n)}{r/\sigma_s} + \frac{c_2(n)}{(r/\sigma_s)^2} - \frac{4 + \alpha}{(r/\sigma_s)^3}, \quad [1]$$

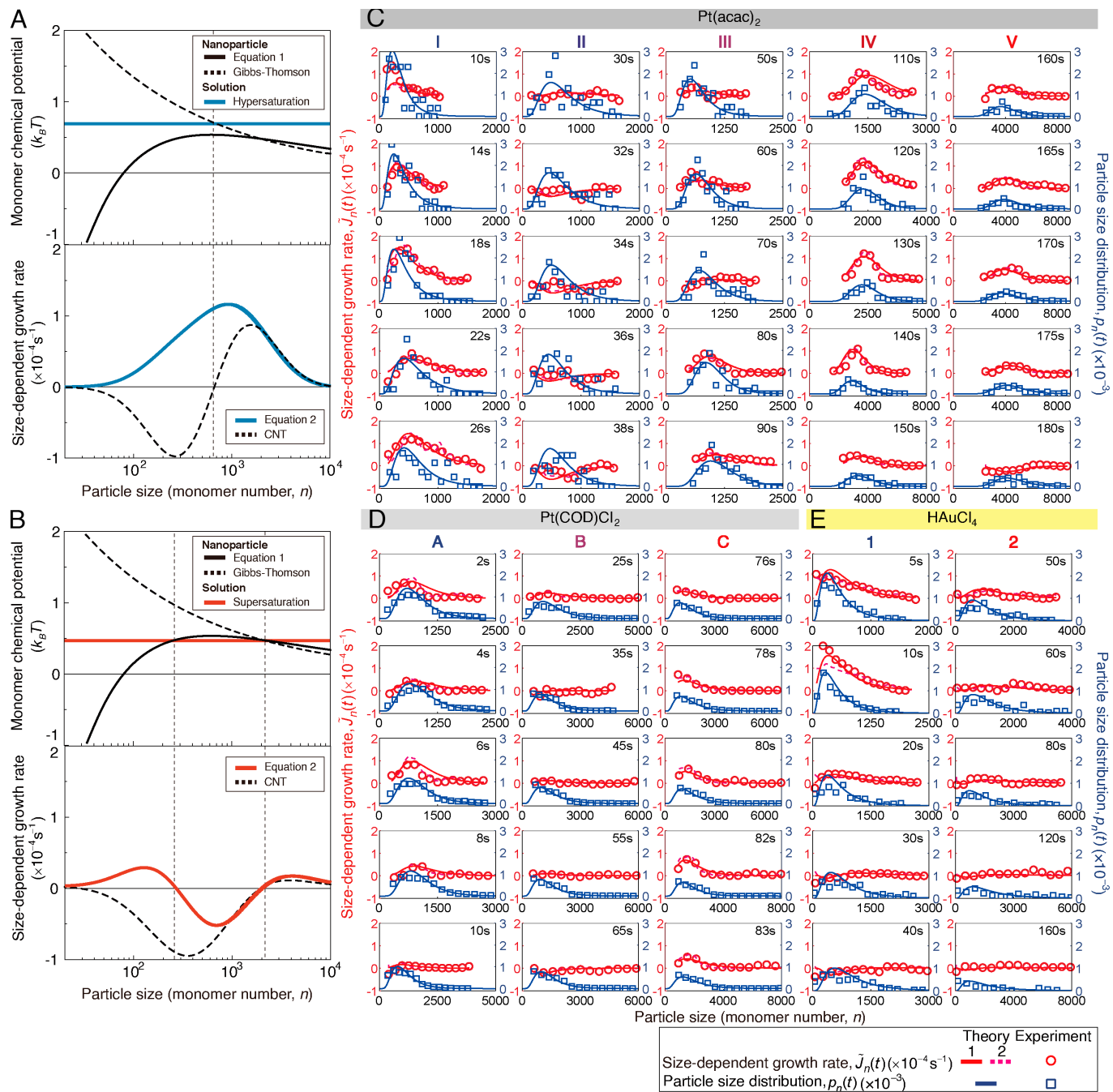


Fig. 2. Size-dependent growth rate and size distribution of nanoparticles at various times. (A and B) (Upper) Chemical potential μ_n^s of monomer in a nanoparticle, Eq. 1 (black solid line), the Gibbs-Thomson equation (dashed line), and chemical potential μ_1 of monomer in solution in supersaturation (blue line) and in supersaturation (red line). (Lower) Size-dependent growth rate $J_n(t)$ given in Eq. 2 scaled by the value of the total monomer density, $\rho_{1,T}(t_0)$, at the beginning of our measurement. The results of Eq. 2: hypersaturation condition (blue line in A) and supersaturation condition (red line in B). The results of the CNT (dashed lines). The size-dependent growth rate $J_n(t)$ has a positive value for nanoparticle size range for which a nanoparticle has a lower chemical potential than the surrounding solution. Our theory predicts that J_n has a positive value for all n under the hypersaturation condition ($\mu_n^s < \mu_1$ for all n) and that J_n can have a negative value for nanoparticles with an intermediate size range satisfying $\mu_n^s > \mu_1$ under the supersaturation condition with μ_1 higher than the chemical potential in a macroscopic crystal (represented by the zero horizontal line) but lower than the maximum chemical potential in a nanoparticle. The CNT predicts Ostwald ripening, where J_n has a negative value for small nanoparticles and a positive value for large nanoparticles, which is inconsistent with our experimental results. (C-E) Comparison made between experimental data (symbols) and results of the present theory (lines) for the scaled size-dependent growth rate $\tilde{J}_n(t) [\equiv J_n(t)/\rho_{1,T}(t_0)]$ (red) and the nanoparticle size distribution $p_n(t)$ (blue). (C) Results for platinum nanoparticles generated from precursor $\text{Pt}(\text{acac})_2$. (D) Results for platinum nanoparticles from precursor $\text{Pt}(\text{COD})\text{Cl}_2$. (E) Results for gold nanoparticles generated from precursor HAuCl_4 . Theoretical results of $\tilde{J}_n(t)$ were calculated from Eq. 2 with $p_n(t)$ from the theoretical result (solid line) or from the experimental data (dashed line) (see *SI Appendix, Text S17* for the calculation method of $\tilde{J}_n(t)$). The result of the modified-lognormal distribution given in *SI Appendix, Materials and Methods, Eq. M10* (blue lines), whose form is completely determined by the first eight moments of the nanoparticle size (Fig. 3).

where β and r denote, respectively, inverse thermal energy $(k_B T)^{-1}$ with k_B and T denoting the Boltzmann constant and temperature, and the effective radius of a nanoparticle. The value of r is related to the monomer number, n , in a nanoparticle by

$n = (r/\sigma_s)^3 [\equiv 4\pi r^3 \rho_s / 3]$ with ρ_s being the monomer number density in the nanoparticle. On the left-hand side of Eq. 1, μ_∞^s designates the chemical potential of monomers in a macroscopic crystal. On the right-hand side (r.h.s.) of Eq. 1, $c_1(n)$ and $c_2(n)$ are

Table 1. Optimized values of the time-independent physicochemical parameters associated with nanoparticle growth

Parameter	$\Delta\epsilon_f$	$\Delta\epsilon_e$	$4 + \alpha$	$\kappa_a\sigma_s/D_1$	$\kappa_a\rho_{1,\infty}(\text{nm}^{-2}\text{s}^{-1})$	$\bar{\delta}$
Pt nanoparticle	3.04	-1.35	6.50	1.71×10^{-1}	1.40	1.76, 1.62
	3.46	-3.07	7.13	3.11×10^{-2}	4.72×10^{-2}	1.73
Au nanoparticle	5.45	-4.06	8.72	4.24×10^{-1}	2.43	1.70
Iron oxide nanoparticle	2.08	-3.17	4.06	6.45×10^{-2}	3.98×10^{-3}	1.67
CdSe nanoparticle	1.24	-1.66	4.17	5.03×10^{-2}	7.68×10^{-3}	1.70

The first three parameters, $\Delta\epsilon_f [\equiv -\ln(q_f/q_b)]$, $\Delta\epsilon_e [\equiv -\ln(q_e/q_b)]$, and $4 + \alpha$ are associated with the chemical potential of monomers in a single nanoparticle (Eq. 1). q_b (q_f or q_e) stands for the electronic partition function of a monomer at a bulk (facial or edge) site of an n -mer. $\Delta\epsilon_f$ ($\Delta\epsilon_e$) denotes the thermal energy-scaled free energy of a monomer at a facial (edge) site with respect to the free energy of a monomer at a bulk site. $\Delta\epsilon_f$ is, in general, positive, while $\Delta\epsilon_e$ can be either positive or negative, depending not only on the type of metal constituting nanoparticles but also on the type of passivating ligand or medium surrounding the nanoparticles. $4 + \alpha$ originate from the translational and rotational motion and the configurational degeneracy of a nanoparticle. The last two parameters, $\kappa_a\sigma_s/D_1$ and $\kappa_a\rho_{1,\infty}$, characterize the rate of diffusion-influenced bimolecular association between monomers and nanoparticles. κ_a and D_1 denote the bimolecular association rate parameter and the monomer diffusion coefficient, respectively. σ_s denotes the radius corresponding to the effective volume occupied by a single monomer inside a nanoparticle, i.e., $\rho_s^{-1} \equiv 4\pi\sigma_s^3/3$ with ρ_s being the monomer number density of the nanoparticle. The value of dimensionless parameter $\kappa_a\sigma_s/D_1$ diverges in the diffusion-controlled limit but vanishes in the activation-controlled limit. $\rho_{1,\infty}$ denotes the monomer solubility. The last parameter, $\bar{\delta}$, indicates the average of shape index values at all times (SI Appendix, Fig. S11). For the platinum nanoparticle, the first and second rows respectively present the parameter values extracted from the in-situ and ex-situ experiments; in the first row, the first and second values of $\bar{\delta}$ were extracted from the experimental systems with precursors Pt(acac)₂ and Pt(COD)Cl₂, respectively. See SI Appendix, Text S6 for further discussion.

size- and shape-dependent parameters, proportional to the free energy difference between the surface and core of a nanoparticle. The third term on the r.h.s. of Eq. 1 originates from the translational and rotational motion and the configurational degeneracy of a nanoparticle (*Materials and Methods*).

The chemical potential of monomers in a nanoparticle given in Eq. 1 has a finite maximum at a critical size, n^\dagger . This nonmonotonic size dependence of the chemical potential qualitatively differs from the Gibbs–Thomson equation underlying the CNT, according to which the chemical potential monotonically decreases with the nanoparticle size.

The nonmonotonic size dependence of the chemical potential in the nanoparticle, along with the time-dependent variation of the chemical potential in solution, causes the size-dependent profile of the growth rate to undergo dramatic shape changes over time (Figs. 1D and 2A and B and SI Appendix, Text S5 and *Materials and Methods*). This is because the growth rate of a nanoparticle depends on the chemical potential difference between the solution and the nanoparticle. The definition of the net growth rate J_n is given by $J_n = k_n^a\rho_1(t)\rho_n(t) - k_{n+1}^d\rho_{n+1}(t)$ ($n \geq 1$), where ρ_n , k_n^a , and k_{n+1}^d denote, respectively, the concentration of n -mers, the rate coefficients of diffusion-influenced monomer association with n -mers and monomer dissociation from $(n+1)$ -mers. Starting from this definition, we derived the exact expression of the

size-dependent growth rate J_n in terms of the difference, $\mu_n^s - \mu_1$, between the chemical potential μ_n^s in a nanoparticle and the chemical potential μ_1 in solution as

$$J_n(t) = k_{n+1}^d\rho_{n+1} \left(e^{-\beta[\mu_n^s - \mu_1(t)]} \rho_n / \rho_{n+1} - 1 \right), \quad (n \geq 1), \quad [2]$$

where $\mu_1(t)$ denotes the chemical potential of monomers in solution. It is established that $\mu_1(t)$ logarithmically increases with monomer concentration, i.e., $\mu_1(t) = \mu_1^\circ + k_B T \ln(\rho_1(t)/\rho^\circ)$ with μ_1° and ρ° being the chemical potential and density of monomer in the standard-state solution, respectively.

According to this formula, nanoparticles with all sizes grow under the supersaturation conditions under which the solution has a higher chemical potential than the nanoparticle in the entire size range, i.e., $\mu_1 > \mu_n^s$ ($1 \leq n < \infty$) (Fig. 2A). This is the case in Phase-I, -III to V of platinum nanoparticles generated from precursor Pt(acac)₂, in Phase-A and -C of platinum nanoparticles from precursor Pt(COD)Cl₂, and in Phase-1 for gold nanoparticles from precursor HAuCl₄ (Fig. 4). On the other hand, under supersaturation conditions under which the chemical potential μ_1 in solution is lower than the maximum chemical potential $\mu_{n^\dagger}^s$ in nanoparticle but higher than the chemical potential μ_∞^s in the macroscopic crystal ($\mu_\infty^s < \mu_1 < \mu_{n^\dagger}^s$) (Fig. 2B), nanoparticles

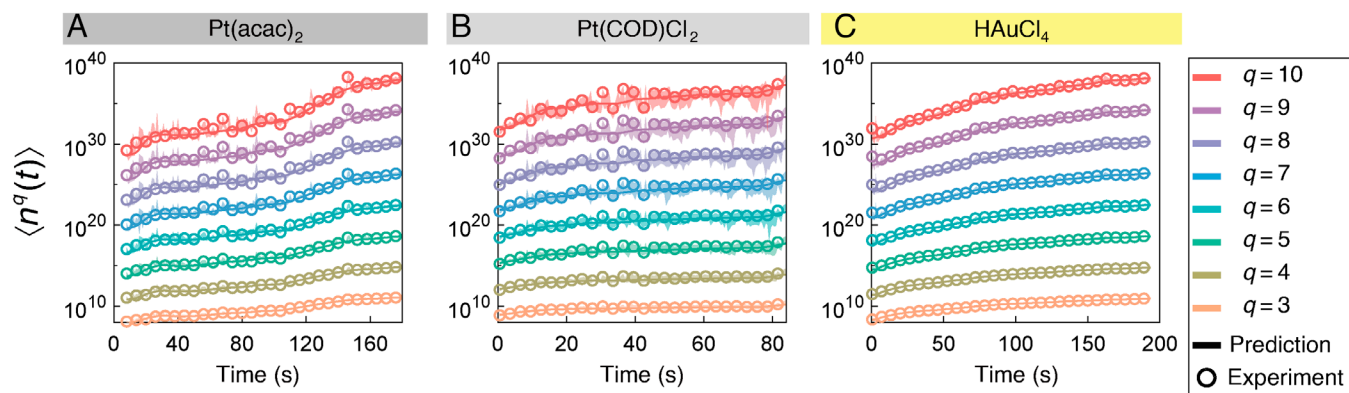


Fig. 3. Comparison between theoretical prediction and experimental results for the higher-order moments of nanoparticle size. The predictions of our theory (lines) and the experimental results (circles) for the third to tenth moments of the nanoparticle size for (A) platinum nanoparticles generated from precursor Pt(acac)₂, (B) platinum nanoparticles generated from precursor Pt(COD)Cl₂, and (C) gold nanoparticles generated from precursor HAuCl₄. SI Appendix, Eqs. S8–18–S8–21 with the optimized parameter values in Table 1 were used to make the theoretical prediction of the higher-order moments, $\langle n^q(t) \rangle$ ($q = 3, \dots, 10$) (SI Appendix, Text S16 and *Materials and Methods*). The agreement between theoretical predictions and experimental results for the higher-order moments of the nanoparticle size corroborates the correctness of our theory and quantitative analysis. The shaded area represents the SD at each time frame, estimated from 1,000 bootstrap-sampled sets.

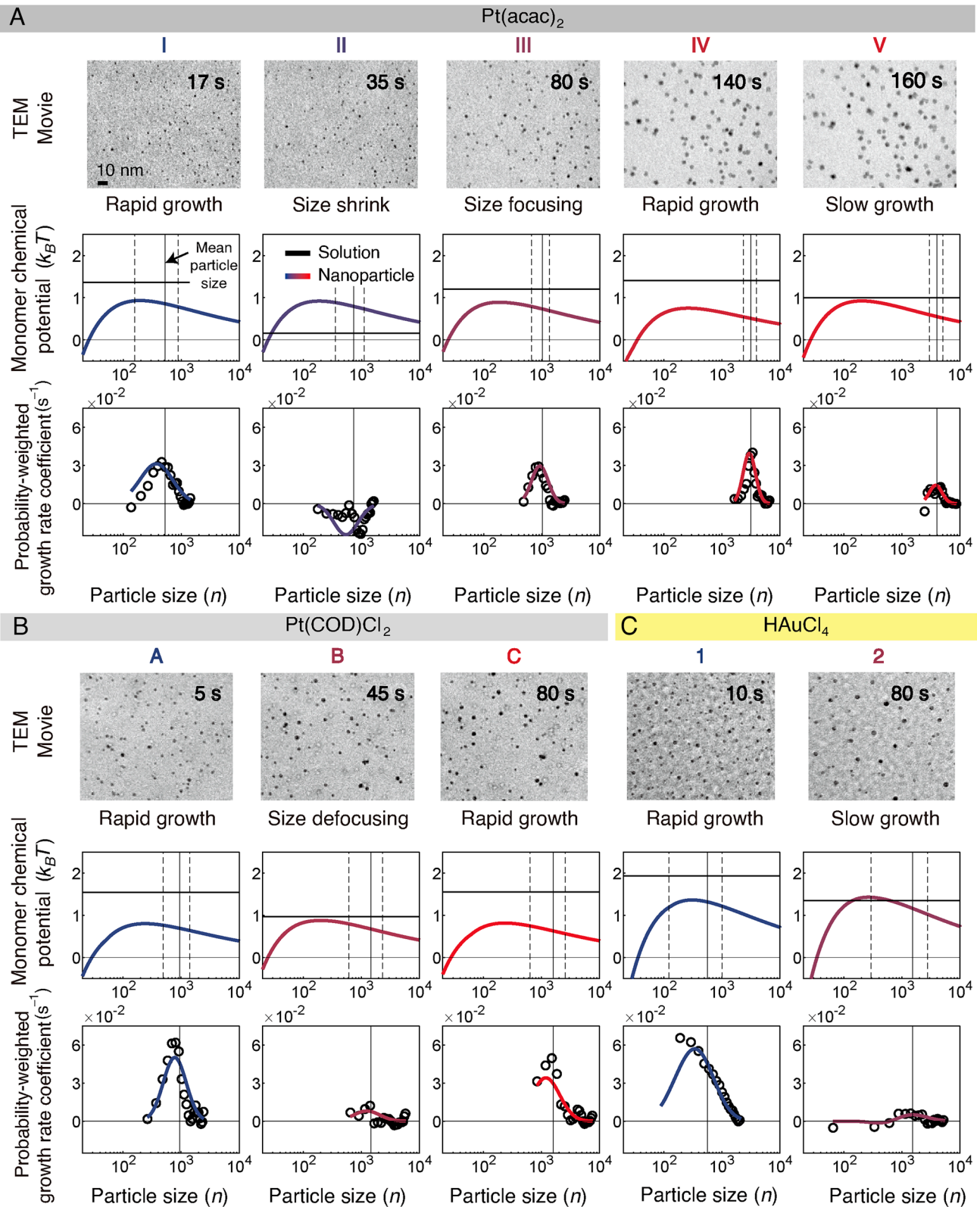


Fig. 4. Phase-dependent dynamics of nanoparticle growth. 1st row: TEM image. 2nd row: Monomer chemical potential, μ_n^s , in nanoparticle phase (colored solid line) and monomer chemical potential, μ_1 , in solution phase (black solid line); the mean particle size (vertical solid line) and error bar (vertical dashed lines). $\mu_n^s - \mu_1(t)$ is the same as $\Delta G_r(n - n + 1) \equiv -k_B T \ln(k_n^a \rho_n / k_{n+1}^d \rho_{n+1})$ (Materials and Methods) or $\Delta G_{n+1} - \Delta G_n (\cong \partial \Delta G_n / \partial n)$, where ΔG_n denotes the free energy change associated with the formation of an n -mer from n monomers (see SI Appendix, Eq. S13-4 and Text S13 for the precise definition of ΔG_n and SI Appendix, Fig. S19 for the time-dependent change of ΔG_n). 3rd row: Probability-weighted growth rate coefficient, $p_n j_n$; experimental data (circles) and theoretical results (colored lines). p_n and j_n denote the nanoparticle size distribution and growth rate coefficient defined by $J_n \equiv j_n / p_n$ (Eq. 2 for J_n and p_n). (A and B) Results for platinum nanoparticles generated from precursor Pt(acac)₂ and from precursor Pt(COD)Cl₂. (C) Results for gold nanoparticles generated from precursor HAuCl₄.

with intermediate sizes, or radius r between r^* and r^{**} in Fig. 1D, shrinks and the growth rates are negative. This results because monomers in these nanoparticles with a higher chemical potential than solution phase would move into the solution with a lower chemical potential. The negative growth rate of intermediate-sized nanoparticles is clearly demonstrated in Phase-II of platinum nanoparticles generated from precursor Pt(acac)₂ (Fig. 4A). These experimental observations cannot be explained by any previous theories based on the Gibbs–Thomson equation. We emphasize that this nonclassical size-dependent growth dynamics is not unique to platinum and gold nanoparticles; instead, it emerges whenever the chemical potential in a nanoparticle has the non-monotonic size dependence.

By analyzing the “time-dependent” experimental data for the size-dependent growth rate and size distribution for in-situ growth of metal nanoparticles under different precursor conditions as well as the time profiles of the solution-phase chemical potential $\mu_1(t)$ extracted from our analysis, we reconstructed the time-independent size dependence of the excess chemical potential, $\mu_n^s - \mu_\infty^s$ (Fig. 5). These reconstructed chemical potential differences are found to be in good agreement with our theory and are independent of the monomer supply rate. This result corroborates the correctness of our theory and analysis. Note here that, for the reconstruction of the time-independent chemical potential from the time-dependent experimental data using Eq. 2, an accurate estimation of the size-dependent growth rate and the size distribution of nanoparticles is required. For this reason, the accuracy of the reconstructed chemical potential is limited for rarely observed small nanoparticles.

In order to demonstrate the broad applicability of our model and theory, we also analyzed experimental data on ex-situ growth of iron oxide and CdSe nanoparticles synthesized using conventional heat-up (5) and hot-injection methods (37), respectively (*Materials and Methods*). We confirmed that our model and theory, without any modifications, provide a quantitative explanation of these ex-situ nanoparticle growth data (*SI Appendix, Fig. S14*). In addition, we conducted ex-situ synthesis of Pt nanoparticles using precursor Pt(acac)₂ and quantitatively analyzed the growth dynamics during the synthesis. The chemical potential parameters extracted from the ex-situ experiment were found to be similar to those extracted from the in-situ experiment conducted with identical solvents, ligands, and precursors (Table 1).

Our quantitative analysis also reveals that all nanoparticles in the systems we investigated maintain a geometry similar to a truncated octahedron across all growth phases, without showing a systematic time dependence (*SI Appendix, Figs. S11 and S12*). This result is consistent with our observation that all tracked nanoparticles exhibit a quasi-spherical morphology within the observation time windows of our in-situ and ex-situ experiments (*Movies S1–S4*).

It is noteworthy that our theory consistently explains diverse experimental observables characterizing complex growth dynamics of platinum nanoparticles synthesized from different monomer precursors, without changing the time-independent microscopic parameters characterizing the platinum nanoparticle (Table 1 for the optimized parameter values). In addition, the present theory provides a unified, quantitative explanation of growth dynamics of three different nanoparticle systems including gold, iron oxide, and CdSe. This demonstrates the wide application range of our nanoparticle model and theory.

Coalescence Growth Dynamics. Nanoparticles also undergo coalescence (Fig. 6A) (21, 29, 30, 38). During coalescence, the size of the nanoparticles in Group-B abruptly increases over a short period of time (Fig. 6B) in contrast with Group-A that grows continuously. Our experimental data show that platinum nanoparticle coalescence transiently occurs only near the end of Phase-III in our experiment with precursor Pt(acac)₂ (Fig. 6C), where monomeric growth is slow and the nanoparticles manifest a small size fluctuation around the mean, i.e., 1.5 nm ± 0.2 nm, because of size focusing throughout Phase-III. Thus, coalescing nanoparticles have similar radii (Fig. 6A and D). Both the coalescence rate coefficient and the coalescence time distribution are unimodal functions of time (Fig. 6C and E). Individual trajectories of coalescing nanoparticles clearly show that the nanoparticles, which undergo random thermal motion, coalesce when their separation becomes approximately 5.87 nm, close to twice the sum of the nanoparticle radius and the ligand length (Fig. 6F and *SI Appendix, Table S1*). This transient coalescence dynamics between growing nanoparticles cannot be explained by the classical chemical kinetics or previously reported diffusion-influenced reaction kinetics for particles with constant size and diffusion coefficient (39). The classical Smoluchowski coagulation kinetics (40) can explain size distributions of silver nanoparticles that grow primarily through aggregation rather than monomeric

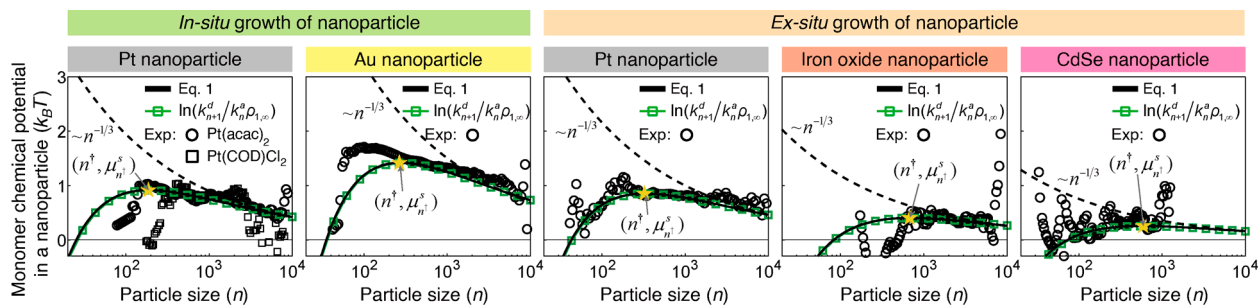


Fig. 5. Chemical potential of colloidal nanoparticle systems. Chemical potential, μ_n^s , in a nanoparticle. (Left) Results for in-situ growth of platinum nanoparticles (1st column) and gold nanoparticles (2nd column). (Right) Results for ex-situ growth of platinum (3rd column), iron oxide nanoparticles (4th column), and CdSe nanoparticles (5th column). The results extracted from the size-dependent growth rate data using Eq. 2: 1st column: Pt(acac)₂ (circles) and Pt(COD)Cl₂ (squares), and other nanoparticles (circles). The result of Eq. 1 with the optimized parameter values in Table 1 (black solid line) and the logarithm of the ratio between k_{n+1}^d and $k_n^d \rho_{1,\infty}$ (green line with squares). The maximum value, $\mu_{n^*}^s$, of the chemical potential at $n = n^*$ is marked by the yellow star: $(n^*, \mu_{n^*}^s/k_B T) = (186, 0.92)$, $(266, 1.41)$, $(678, 0.40)$, and $(592, 0.26)$ for platinum, gold, iron oxide, and CdSe nanoparticle systems. For platinum nanoparticles synthesized in the ex-situ experiment, $(n^*, \mu_{n^*}^s/k_B T) = (323, 0.85)$. See also *SI Appendix, Fig. S20* for the dependence of μ_n^s on the model parameters. The result of the Gibbs–Thomson equation (dashed line). k_n^a , k_{n+1}^d , and $\rho_{1,\infty}$ denote the rate coefficients of monomer association with n -mers and dissociation from $(n+1)$ -mers, and the solubility of monomers, respectively.

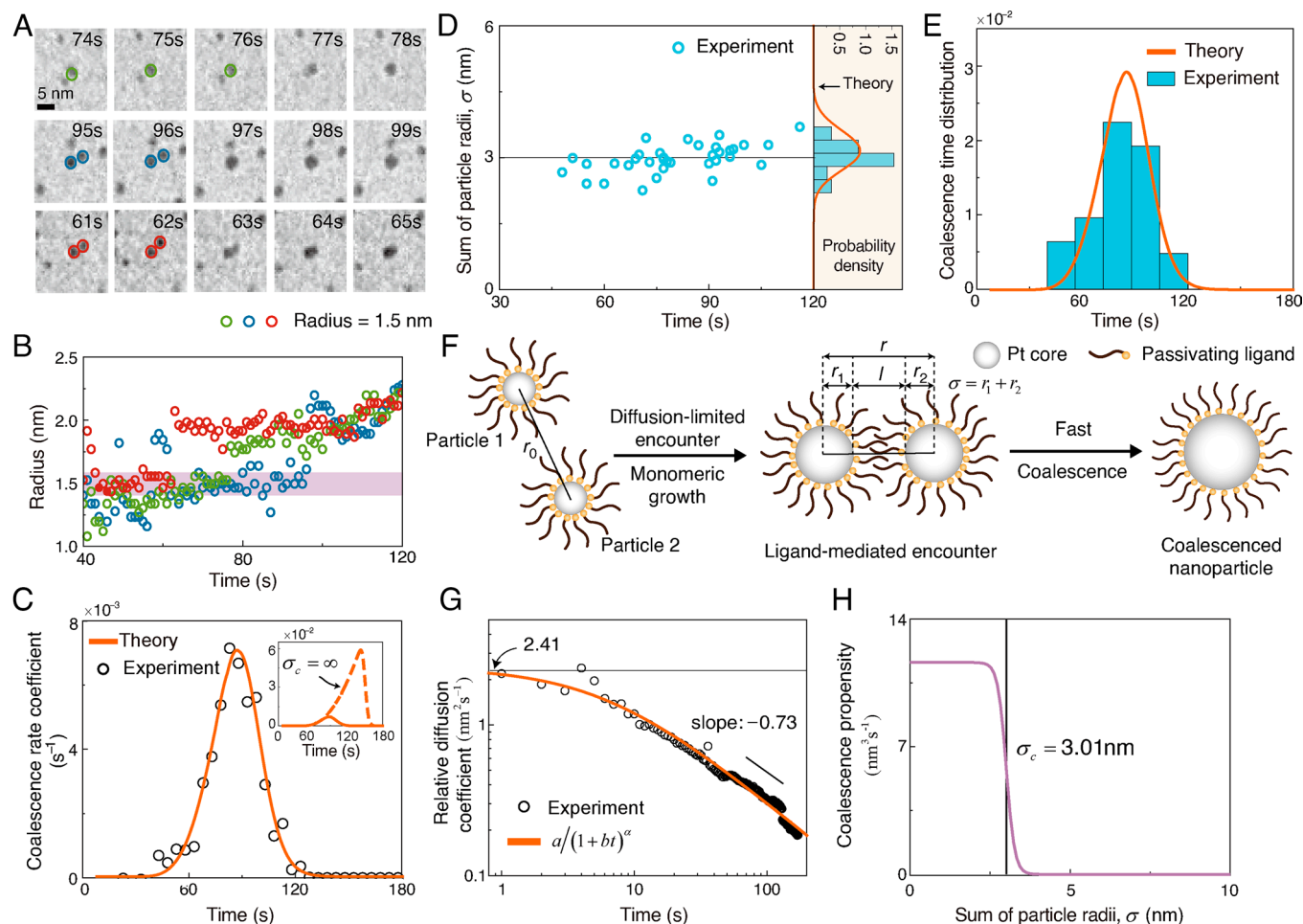


Fig. 6. Transient chemical dynamics of nanoparticle coalescence occurring within a specific nanoparticle size range. (A) TEM images showing three representative coalescence events. Circle: 1.5 nm. (Scale bar: 5 nm.) (B) Time-dependent radii of the three nanoparticles shown in A. Coalescence predominantly occurs when the nanoparticle radius is about 1.5 nm regardless of coalescing times (see also *SI Appendix, Fig. S21* for a discussion on post-coalescence growth). (C) Time-dependent coalescence rate coefficient: theoretical results (solid line) and experimental data (circles). Inset: Coalescence rate coefficient calculated for hypothetical nanoparticle model with a size-independent coalescence propensity (dashed line). (D) Coalescence time and sum of nanoparticle radii, σ , at each coalescence event. (Right) Probability density of σ : experimental data (bars) and theoretical prediction (solid line). (E) Coalescence time distribution: theoretical results (solid line) and experimental data (bar). (F) Schematic of the nanoparticle coalescence process. (G) Relative diffusion coefficient between a pair of growing nanoparticles. The diffusion coefficient decreases with time, following a power-law behavior, $1/t^{0.73}$, at long times because the mean nanoparticle radius, inversely proportional to the diffusion coefficient, exhibits a power-law increase with a similar exponent over the same time period (*SI Appendix, Fig. S15*). (H) Size-dependent coalescence propensity extracted from our analysis. The coalescence propensity becomes vanishingly small for nanoparticles with values of σ far greater than 3.0 nm.

addition (41). However, this theory is inapplicable to Group-B in which nanoparticles grow through both monomeric addition and coalescence (*SI Appendix, Fig. S15*), during which the nanoparticle size, and consequently, the diffusion coefficient change over time.

We found it essential to account for two facts in understanding the transient coalescence dynamics. First, nanoparticles are initially separated by a distance far greater than their encounter distance, and second, growing nanoparticles undergo anomalous thermal motion because their diffusion coefficient, inversely proportional to the nanoparticle size, decreases with time (Fig. 6G). In addition, to achieve a quantitative explanation of our experimental data, we assume that the coalescence propensity of nanoparticles greater than a particular size rapidly decreases with size (Fig. 6H). To obtain a mathematical description of this coalescence model, we extended the reduced distribution function formalism, developed for the diffusion-influenced bimolecular reactions (42, 43), to encompass growing nanoparticle systems (*Materials and Methods*). The resulting kinetic equation successfully explains the time profiles of the coalescence rate coefficient and the distribution of coalescence time. According to our analysis, the onset of coalescence is delayed because it takes time for initially separated

nanoparticle pairs to form reactive encounter pairs via thermal motion. The coalescence time distribution is dependent on the system properties including initial nanoparticle density, reactivity, and monomeric growth dynamics of nanoparticles (*SI Appendix, Fig. S16*). The coalescence rate vanishes at times longer than 126 s not only because the larger nanoparticles have a smaller diffusion-influenced rate but also because they have a vanishingly small coalescence propensity.

Discussion

The formation Gibbs free energy, or Gibbs free energy change ΔG_n associated with the formation of an n -mer from n monomers, shows a qualitative shape transition depending on the chemical potential difference between solution and nanoparticle phases. When the chemical potential in the solution is higher than the maximum chemical potential in the nanoparticle, ΔG_n monotonically decreases with nanoparticle size across the entire size range. On the other hand, when the chemical potential in solution is lower than the maximum chemical potential in nanoparticle but higher than the chemical potential in the macroscopic crystal,

ΔG_n has a minimum at a finite size r^* and a barrier at a larger size r^{**} (Fig. 1D). This monomer-concentration-dependent ΔG_n profile dynamics is essential in quantitative understanding of complex growth dynamics of various nanoparticle systems, which is in stark contrast with the widely accepted formation free energy profile with a single barrier in the CNT.

The CNT based on the Gibbs–Thomson equation does provide a useful, approximate result for the crystallization rate (44); however, by considering the strongly nonextensive free energy terms, overlooked in the CNT, Dillmann and Meier explained the nucleation-rate data more accurately than the CNT (45, 46). Our result for the chemical potential in a nanoparticle has the similar size dependence to the Gibbs–Thomson equation when the particle size is large enough. However, for small nanoparticles, the chemical potential in the nanoparticle has a strongly nonmonotonic size dependence, which has a direct consequence on the size-dependent growth dynamics of nanoparticles. Fig. 2A and B demonstrate the nonclassical growth dynamics of nanoparticles under hypersaturation and supersaturation conditions, respectively. Under the hypersaturation condition, monomers in solution have a higher chemical potential than in nanoparticles of all sizes, resulting in a positive growth rate across all sizes. In contrast, under the supersaturation condition, monomers in solution have a lower chemical potential than monomers in a nanoparticle with intermediate size, or with radius between r^* and r^{**} in Fig. 1D, leading to a negative growth rate of the nanoparticle.

The nonclassical growth dynamics is a generic feature of small colloidal nanoparticles. The nonmonotonic size dependence of the chemical potential results from stronger ligand binding at edge and vertex sites relative to facial sites (47), along with contributions from translational and rotational motion, and configurational degeneracy of the nanoparticles (SI Appendix, Text S6). Their contributions increase as the nanoparticle size decreases. For this reason, the nonmonotonic size dependence of the chemical potential and the resulting nonclassical size-dependent growth dynamics are observed across various small nanoparticle systems we investigated.

There exists a general relationship among the time-dependent mean and variance of nanoparticle size and the size-dependent growth rates (SI Appendix, Materials and Methods). We find this relationship consistent with the Chemical Fluctuation Theorem governing gene expression in living cells (48). Based on this relationship, we could provide a straightforward physical explanation of the stronger size-focusing dynamics of nanoparticles under the faster monomer supply condition observed in our experiment (SI Appendix, Fig. S17). This observation is also consistent with the previously reported experimental results in ref. 49.

This work provides insights for designing controlled nanoparticle synthesis. For example, the size distribution of Group-A undergoing monomeric growth is narrower than that of Group-B accompanying coalescence (SI Appendix, Fig. S18). This suggests that a synthetic approach that drives more particles to follow the monomeric growth pathway will enhance the monodispersity of the synthesized nanoparticles.

Currently, the real-time dynamics of nanoparticle size and growth rate of individual colloidal nanoparticles can only be monitored through in-situ liquid-phase TEM experiments. However, it is not easy to control the monomer supply rate precisely in the TEM experiments. Using our model and theory with optimized parameters values, it is possible to predict the time-dependent nanoparticle size distribution and the size-dependent growth dynamics at various monomer supply rates, temperatures, and other experimental conditions, which would be useful for optimizing the

experimental conditions for a desired size distribution or growth dynamics of nanoparticles.

Our theory enables one to predict the size-dependent growth rate and the size distribution of a nanoparticle system, given that the size-dependent chemical potential μ_n^s , or free energy f_n^s , and the diffusion-influenced monomer association rate coefficient k_n^a are available for the nanoparticle system. These quantities can be calculated by combining statistical thermodynamics of mesoscopic systems with modern computational sciences including machine learning, which presents an exciting avenue for further exploration.

Finally, our theory can be extended to investigate nucleation and growth dynamics of more complex systems. Zheng and coworkers showed that, at short times, all low-index facets of platinum nanoparticles exhibit similar growth rates, but at long times beyond our current experimental observation time window, the {100} facets stop growing while the other facets keep growing, resulting in the formation of cube-shaped nanoparticles at long times (31). To explain these phenomena, it is necessary to consider the facet dependence of the monomer association rate and the monomer chemical potential in a nanoparticle. Similarly, Haji-Akbari and Debenedetti reported that ice crystallization occurs through geometry-dependent nucleation mechanisms and dynamics (50). It has also been demonstrated that dynamic structural changes have a critical impact on the ice crystallization in supercooled water (51) or the dissolution of amorphous silica (52). In addition, recent studies showed that crystallization in calcium carbonate and protein solutions occurs through multistage pathways involving an intermediate condensed phase (53–55), and that the size of perovskite nanocrystals formed in cesium lead halide solution is controlled by the halide ion concentration in the solution (56). The present model and theory can be extended to encompass these systems, which we leave for future investigation.

Materials and Methods

Experimental Section. In-situ liquid-phase cell TEM measurement was performed to obtain TEM images of growing platinum and gold nanoparticles. For platinum nanoparticles, the TEM measurement was repeatedly performed using two different precursors, Pt(acac)₂ and Pt(COD)Cl₂, with different monomer supply rates. Ex-situ growth study was also performed for platinum, cadmium selenide, and iron oxide nanoparticles. More details about these experiments are presented in the SI Appendix, Materials and Methods.

Theory Section. Eq. 1 is derived by applying statistical thermodynamics of a canonical ensemble to our nanoparticle model. Eq. 2 is derived from the definition of the net growth rate and the detailed balance condition established in chemical kinetics and statistical thermodynamics. Simultaneous quantitative analyses of the mean and variance of the nanoparticle size and the size-dependent growth rate of Group-A nanoparticles were performed at all times investigated, based on Eqs. 1 and 2, and the hierarchical kinetic equations describing diffusion-influenced reversible association of nanoparticles. To describe diffusion-influenced coalescence between growing nanoparticles, we extended Lee and Karplus's reduced distribution function formalism for diffusion-influenced reactions between molecules (42, 43). More details are presented in the SI Appendix, Materials and Methods.

Data, Materials, and Software Availability. Experimental data and matlab codes data have been deposited in GitHub (https://github.com/JGKang92/Nanoparticle_Growth) (57).

ACKNOWLEDGMENTS. This work is supported by Global Science Research Center Program (RS-2024-00411134), Creative Research Initiative Project Program (RS-2015-NR011925), and Engineering Research Center Program (NRF-2020R1A5A1018052) funded by the National Research Foundation (NRF) of Korea (J.S.); IBS-R006-D1 (T.H. and J.P.); NRF grant funded by the

Korea government (Ministry of Science and ICT (MSIT)) RS-2024-00449965 and RS-2024-00421181 (J.P.); NRF grant funded by the Korea government (MSIT) NRF-2020R1A2C1102788 (J.-H.K.); NRF grant funded by the Korea government NRF-2021R1C1C1014339 (B.H.K.); NRF grant funded by the Korea government (MSIT) 2022R1A4A3031263 (W.C.L.); Research fund of Hanyang University HY-2018-N (S.J. and W.C.L.); Global Frontier Program through the Global Frontier Hybrid Interface Materials of the NRF of Korea funded by the Ministry of Science and ICT 2013M3A6B107888 (B.H.); Samsung Science and Technology Foundation under project number S5TF-BA2302-06 (J.R. and J.P.).

Author affiliations: ^aDepartment of Chemistry, Global Science Research Center for Systems Chemistry, Chung-Ang University, Seoul 06974, Republic of Korea; ^bDepartment of Chemistry, Creative Research Initiative Center for Chemical Dynamics in Living Cells, Chung-Ang University, Seoul 06974, Republic of Korea; ^cDepartment of Chemistry, Chung-Ang University, Seoul 06974, Republic of Korea; ^dCenter for Nanoparticle Research, Institute for Basic Science, Seoul 08826, Republic of Korea; ^eSchool of Chemical and Biological Engineering, and Institute of Chemical Process, Seoul National University, Seoul 08826, Republic of Korea; ^fDepartment of Materials Science and Engineering, Soongsil University,

Seoul 06978, Republic of Korea; ^gDepartment of Chemical and Biomolecular Engineering, University of California, Berkeley, CA 94720; ^hChemical Sciences Division, Lawrence Berkeley National Laboratory, Berkeley, CA 94720; ⁱDepartment of Chemistry, National Institute of Innovative Functional Imaging, Chung-Ang University, Seoul 06974, Republic of Korea; ^jDepartment of Chemical and Biomolecular Engineering, Yonsei University, Seoul 03722, Republic of Korea; ^kDepartment of Mechanical Engineering, Brain Korea 21 FOUR Education Research Industry Cluster at Ansan-Advanced Materials, Components, Manufacturing Equipment Research Center, Hanyang University, Ansan, Gyeonggi 15588, Republic of Korea; ^lInstitute of Engineering Research, College of Engineering, Seoul National University, Seoul 08826, Republic of Korea; and ^mAdvanced Institute of Convergence Technology, Seoul National University, Suwon, Gyeonggi 16229, Republic of Korea

Author contributions: J. Kim, B.H.K., S.J., W.C.L., T.H., and J.P. designed the experimental research; J.-H.K., S.S., and J.S. designed the theoretical research; B.H.K., Y.S., and J.P. captured the TEM movies; J. Kim conducted the image binarization; J. Kim, J.J., and K.P. conducted the particle tracking; J. Kim, B.H.K., H. Choi, H. Cho, and J.W.J. conducted ex-situ experiments; J. Kim, B.H.K., H. Choi, S.J., B.H., W.C.L., D.K., and J.P. conducted the image analysis of experimental data; J.S. derived equations (1) and (2), developing the theory of nucleation, size focusing, and defocusing of nanoparticles; J.-H.K. and J.S. developed the quantitative analysis methods of the experimental results; J.-H.K., S.S., J. Kang, D. Kim, and M.L. performed the quantitative analysis of the experimental data; J.-H.K., J. Kim, B.H.K., S.S., T.H., J.S., and J.P. wrote the manuscript; T.H. and J.P. supervised the experimental research; J.S. supervised the theoretical research. All authors contributed to the discussion of results.

1. D. V. Talapin, J.-S. Lee, M. V. Kovalenko, E. V. Shevchenko, Prospects of colloidal nanocrystals for electronic and optoelectronic applications. *Chem. Rev.* **110**, 389–458 (2010).
2. M. V. Kovalenko *et al.*, Prospects of nanoscience with nanocrystals. *ACS Nano* **9**, 1012–1057 (2015).
3. M. A. Boles, D. Ling, T. Hyeon, D. V. Talapin, The surface science of nanocrystals. *Nat. Mater.* **15**, 141–153 (2016).
4. C. Murray, D. J. Norris, M. G. Bawendi, Synthesis and characterization of nearly monodisperse CdE (E = sulfur, selenium, tellurium) semiconductor nanocrystallites. *J. Am. Chem. Soc.* **115**, 8706–8715 (1993).
5. J. Park *et al.*, Ultra-large-scale syntheses of monodisperse nanocrystals. *Nat. Mater.* **3**, 891–895 (2004).
6. N. Tian, Z.-Y. Zhou, S.-G. Sun, Y. Ding, Z. L. Wang, Synthesis of tetrahedral platinum nanocrystals with high-index facets and high electro-oxidation activity. *Science* **316**, 732–735 (2007).
7. Y. Shirasaki, G. J. Supran, M. G. Bawendi, V. Bulović, Emergence of colloidal quantum-dot light-emitting technologies. *Nat. Photonics* **7**, 13–23 (2013).
8. L. Liu, A. Corma, Metal catalysts for heterogeneous catalysis: From single atoms to nanoclusters and nanoparticles. *Chem. Rev.* **118**, 4981–5079 (2018).
9. N. T. Thanh, N. Maclean, S. Mahidine, Mechanisms of nucleation and growth of nanoparticles in solution. *Chem. Rev.* **114**, 7610–7630 (2014).
10. J. Lee, J. Yang, S. G. Kwon, T. Hyeon, Nonclassical nucleation and growth of inorganic nanoparticles. *Nat. Rev. Mater.* **1**, 16034 (2016).
11. Z. Ou, Z. Wang, B. Luo, E. Luijten, Q. Chen, Kinetic pathways of crystallization at the nanoscale. *Nat. Mater.* **19**, 450–455 (2020).
12. M. Volmer, A. Weber, Keimbildung in übersättigten Gebilden. *Z. Phys. Chem.* **119**, 277–301 (1926).
13. L. Farkas, Keimbildungsgeschwindigkeit in übersättigten Dämpfen. *Z. Phys. Chem.* **125**, 236–242 (1927).
14. R. Becker, W. Döring, Kinetische behandlung der keimbildung in übersättigten dämpfen. *Ann. Phys.* **416**, 719–752 (1935).
15. J. Hong *et al.*, Metastable hexagonal close-packed palladium hydride in liquid cell TEM. *Nature* **603**, 631–636 (2022).
16. V. K. LaMer, R. H. Dinegar, Theory, production and mechanism of formation of monodispersed hydrosols. *J. Am. Chem. Soc.* **72**, 4847–4854 (1950).
17. X. Peng, J. Wickham, A. Alivisatos, Kinetics of II-VI and III-V colloidal semiconductor nanocrystal growth: “focusing” of size distributions. *J. Am. Chem. Soc.* **120**, 5343–5344 (1998).
18. J. Frenkel, A general theory of heterophase fluctuations and pretransition phenomena. *J. Chem. Phys.* **7**, 538–547 (1939).
19. M. Williamson, R. Tromp, P. Vereecken, R. Hull, F. Ross, Dynamic microscopy of nanoscale cluster growth at the solid-liquid interface. *Nat. Mater.* **2**, 532–536 (2003).
20. H.-G. Liao, L. Cui, S. Whitelam, H. Zheng, Real-time imaging of Pt3Fe nanorod growth in solution. *Science* **336**, 1011–1014 (2012).
21. J. M. Yuk *et al.*, High-resolution EM of colloidal nanocrystal growth using graphene liquid cells. *Science* **336**, 61–64 (2012).
22. B. Luo *et al.*, Unravelling crystal growth of nanoparticles. *Nat. Nanotechnol.* **18**, 589–595 (2023).
23. D. Li *et al.*, Direction-specific interactions control crystal growth by oriented attachment. *Science* **336**, 1014–1018 (2012).
24. J. J. De Yoreo *et al.*, Crystallization by particle attachment in synthetic, biogenic, and geologic environments. *Science* **349**, aaa6760 (2015).
25. N. D. Loh *et al.*, Multistep nucleation of nanocrystals in aqueous solution. *Nat. Chem.* **9**, 77–82 (2017).
26. J. Yang *et al.*, Formation of two-dimensional transition metal oxide nanosheets with nanoparticles as intermediates. *Nat. Mater.* **18**, 970–976 (2019).
27. G. Zhu *et al.*, Self-similar mesocrystals form via interface-driven nucleation and assembly. *Nature* **590**, 416–422 (2021).
28. W. Dachraoui, T. R. Henninen, D. Keller, R. Erni, Multi-step atomic mechanism of platinum nanocrystals nucleation and growth revealed by in-situ liquid cell STEM. *Sci. Rep.* **11**, 23965 (2021).
29. H. Zheng *et al.*, Observation of single colloidal platinum nanocrystal growth trajectories. *Science* **324**, 1309–1312 (2009).
30. H.-G. Liao, H. Zheng, Liquid cell transmission electron microscopy study of platinum iron nanocrystal growth and shape evolution. *J. Am. Chem. Soc.* **135**, 5038–5043 (2013).
31. H.-G. Liao *et al.*, Facet development during platinum nanocube growth. *Science* **345**, 916–919 (2014).
32. D. V. Talapin, A. L. Rogach, M. Haase, H. Weller, Evolution of an ensemble of nanoparticles in a colloidal solution: Theoretical study. *J. Phys. Chem. B* **105**, 12278–12285 (2001).
33. J. Baumgartner *et al.*, Nucleation and growth of magnetite from solution. *Nat. Mater.* **12**, 310–314 (2013).
34. W. J. Habraken *et al.*, Ion-association complexes unite classical and non-classical theories for the biomimetic nucleation of calcium phosphate. *Nat. Commun.* **4**, 1507 (2013).
35. J. Y. Rempel, M. G. Bawendi, K. F. Jensen, Insights into the kinetics of semiconductor nanocrystal nucleation and growth. *J. Am. Chem. Soc.* **131**, 4479–4489 (2009).
36. D. Bradley, G. Roth, Adaptive thresholding using the integral image. *J. Graph. Tools.* **12**, 13–21 (2007).
37. O. Chen *et al.*, Synthesis of metal-selenide nanocrystals using selenium dioxide as the selenium precursor. *Angew. Chem. Int. Ed. Engl.* **47**, 8638–8641 (2008).
38. F. Wang, V. N. Richards, S. P. Shields, W. E. Buhro, Kinetics and mechanisms of aggregative nanocrystal growth. *Chem. Mater.* **26**, 5–21 (2014).
39. S. A. Rice, *Diffusion-Limited Reactions* (Elsevier, 1985).
40. M. V. Smoluchowski, Drei Vorträge über Diffusion, Brownsche Bewegung und Koagulation von Kolloidteilchen. *Phys. Z.* **17**, 585–599 (1916).
41. T. J. Woehl *et al.*, Direct observation of aggregative nanoparticle growth: Kinetic modeling of the size distribution and growth rate. *Nano Lett.* **14**, 373–378 (2014).
42. S. Lee, M. Karplus, Kinetics of diffusion-influenced bimolecular reactions in solution. I. General formalism and relaxation kinetics of fast reversible reactions. *J. Chem. Phys.* **86**, 1883–1903 (1987).
43. J. Sung, S. Lee, Nonequilibrium distribution function formalism for diffusion-influenced bimolecular reactions: Beyond the superposition approximation. *J. Chem. Phys.* **111**, 796–803 (1999).
44. L. Lupi *et al.*, Role of stacking disorder in ice nucleation. *Nature* **551**, 218–222 (2017).
45. A. Dillmann, G. Meier, A refined droplet approach to the problem of homogeneous nucleation from the vapor phase. *J. Chem. Phys.* **94**, 3872–3884 (1991).
46. S. Prestipino, A. Laio, E. Tosatti, Systematic improvement of classical nucleation theory. *Phys. Rev. Lett.* **108**, 225701 (2012).
47. R. Ye *et al.*, Nanoscale cooperative adsorption for materials control. *Nat. Commun.* **12**, 4287 (2021).
48. S. J. Park *et al.*, The chemical fluctuation theorem governing gene expression. *Nat. Commun.* **9**, 297 (2018).
49. S. G. Kwon *et al.*, Kinetics of monodisperse iron oxide nanocrystal formation by “heating-up” process. *J. Am. Chem. Soc.* **129**, 12571–12584 (2007).
50. A. Haji-Akbari, P. G. Debenedetti, Direct calculation of ice homogeneous nucleation rate for a molecular model of water. *Proc. Natl. Acad. Sci. U.S.A.* **112**, 10582–10588 (2015).
51. E. B. Moore, V. Molinero, Structural transformation in supercooled water controls the crystallization rate of ice. *Nature* **479**, 506–508 (2011).
52. P. M. Dove, N. Han, A. F. Wallace, J. J. De Yoreo, Kinetics of amorphous silica dissolution and the paradox of the silica polymorphs. *Proc. Natl. Acad. Sci. U.S.A.* **105**, 9903–9908 (2008).
53. K. Henzler *et al.*, Supersaturated calcium carbonate solutions are classical. *Sci. Adv.* **4**, eaaa6283 (2018).
54. G. A. Tribello, F. Bruneval, C. Liew, M. Parrinello, A molecular dynamics study of the early stages of calcium carbonate growth. *J. Phys. Chem. B* **113**, 11680–11687 (2009).
55. P. R. ten Wolde, D. Frenkel, Enhancement of protein crystal nucleation by critical density fluctuations. *Science* **277**, 1975–1978 (1997).
56. Y. Dong *et al.*, Precise control of quantum confinement in cesium lead halide perovskite quantum dots via thermodynamic equilibrium. *Nano Lett.* **18**, 3716–3722 (2018).
57. S. Song, J. Kang, Nanoparticle_Growth. GitHub. https://github.com/JGKang92/Nanoparticle_Growth. Deposited 29 April 2025.